Morphology-Dependent Stimulated Emission and Field Emission of Ordered CdS Nanostructure Arrays

Tianyou Zhai,[†,‡] Xiaosheng Fang,[‡] Yoshio Bando,[‡] Qing Liao,[†] Xijin Xu,[‡] Haibo Zeng,[‡] Ying Ma,[†,*] Jiannian Yao,[†,*] and Dmitri Golberg[‡]

[†]Beijing National Laboratory for Molecular Sciences (BNLMS), Institute of Chemistry, Chinese Academy of Sciences, Beijing 100190, People's Republic of China, and [‡]World Premier International Center for Materials Nanoarchitectonics (MANA), National Institute for Materials Science (NIMS), Namiki 1-1, Tsukuba, Ibaraki 305-0044, Japan

ABSTRACT   Highly ordered CdS nanostructure arrays were successfully fabricated *via* a simple two-step metal-organic chemical vapor deposition process. Both stimulated emission and field-emission measurements were carried out in an attempt to understand the correlation between the morphologies, alignments, and emission performances of five ordered CdS nanostructure array types (well-aligned truncated nanocones, nanorods, cleft nanorods, quasi-aligned nanowires, and nanowires). The 1D CdS nanostructures of various types displayed notable differences in stimulated and field-emission performances. The stimulated emission strongly correlated with the structure alignment: the better the alignment, the lower the threshold. Both of the alignments and aspect ratios greatly affected the field-emission properties; the CdS emitters of higher aspect ratio and better alignment exhibited better field-emission performance. Thus the well-aligned CdS nanorod arrays had the lower threshold for stimulated emission, and quasi-aligned nanowire arrays produced the higher field-emission current and possessed the lower turn-on fields.

Well-aligned semiconductor nanowires and nanorods have attracted increasing attention due to their unique properties and applications in novel electronic, optoelectronic, and electromechanical nanodevices,[1,2] such as field emitters,[3,4] solar cells,[5] lasers diodes,[6,7] field-effect transistors,[8] sensors,[9] and piezo nanogenerators.[10,11] Considerable efforts have been made with respect to the growth of various semiconductor nanostructure arrays *via* chemical or physical routes in a controlled way. To date, well-aligned nanowire/nanorod arrays have been obtained for the group IV (Si and Ge),[12] groups III−V (GaP, GaAs, and InP),[13] and groups II−VI (ZnO) semiconductors.[14−16] As an important II−VI semiconductor compound, CdS (with band gap energy of 2.52 eV) has been considered as a perspective optoelectronic material for utilization in nonlinear optical devices, flat panel displays, light-emitting diodes, laser, logic gates, transistors, *etc*.[17−19] It is also a good active optical waveguide material and electrically driven lasing material, which may find wide applications in telecommunications, data storage, and near-field optical lithography.[20,21] Synthesis of aligned nanowire arrays is a critical step toward enhancing nanostructure performances in nanoscale devices. However, few CdS nanowire and nanorod arrays have so far been synthesized using thermal evaporation,[22,23] template-assisted growth,[24] and liquid reaction processes.[25,26] It still remains a challenge to synthesize high-quality morphology-tunable CdS nanowires and nanorods at a high yield *via* an effective and low cost method.

In recent years, the research on stimulated emission and field-emission properties of 1D wide-band semiconductors became forefront due to growing demands of micro/nanotechnologies. However, most of the studies have been limited to the analyses of various measurement conditions on lasing and field emission of a single material, while little attention has been paid to the relationship between the nature of a nanostructure and its stimulated/field-emission properties. Variations in such properties are expected even for an individual nanostructure under different dimensions. Morphological variations may also have pronounced effects. According to the Fowler−Nordheim (F−N) theory,[27] the field emission is related to two essential parameters, namely, the work function of an emitting material and the field-enhancement factor.[28] The intrinsic work function is an important parameter that varies mainly from 1 to 7 eV for most of the inorganic semiconductors, the lower being better for the higher emission efficiency.[29]
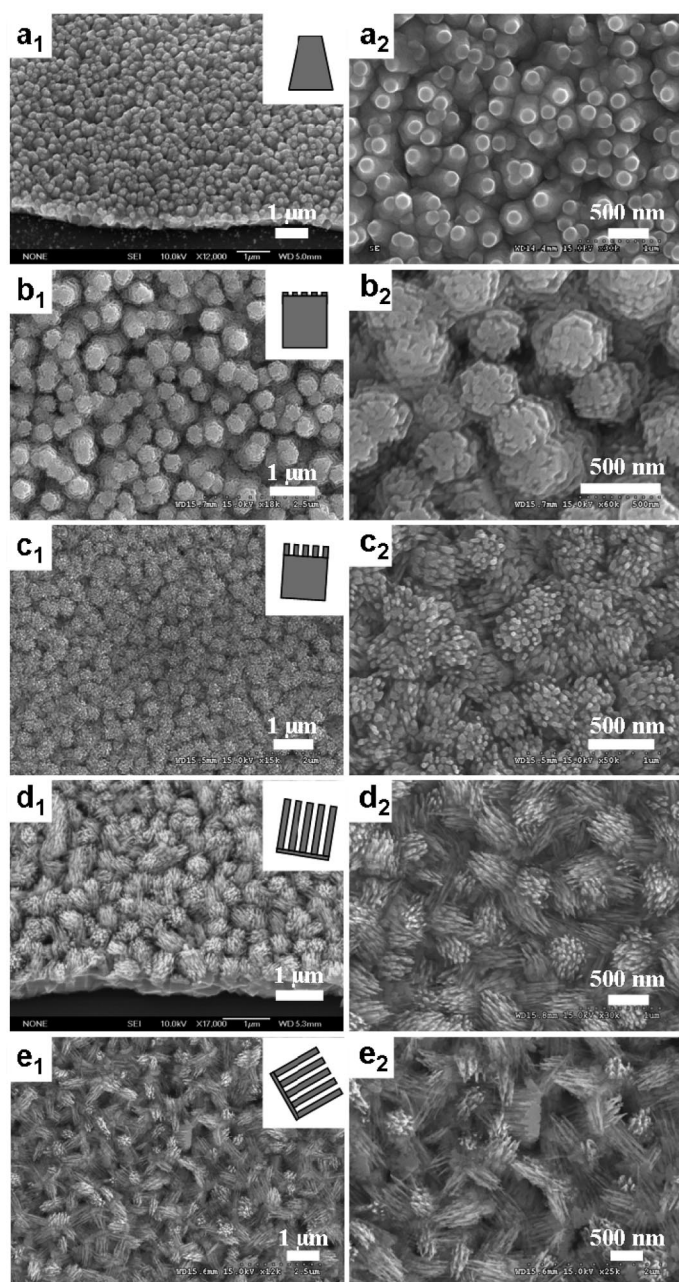
Figure 1. Typical FESEM images and the corresponding geometric sketches of several CdS nanostructures: (a) well-aligned truncated nanocone arrays (sample a); (b) well-aligned nanorod arrays (sample b); (c) well-aligned cleft nanorod arrays (sample c); (d) quasi-aligned nanowire arrays (sample d); and (e) nanowire arrays (sample e).

The field-enhancement factor is defined as the ratio of a local field to an applied field and determined by the shape and morphology of an emitter. Thus, it is possible to achieve strong field emission from a given nanostructured material if it is long and sharp. The tip sharpness may be different, for instance, round closed tips, blunt ends, or conical tips have all been documented. Yu et al. prepared and compared the field-emission performances of three differently shaped ZnO arrays. Among them, the nanoneedle arrays possessed much better field-emission performances than arrays of nanocavities and nanobottles,[30] which was attributed to the

1D shapes and tip sharpness of the array components. Lu et al. investigated the composition effects on the field-emission properties of $Cd_xZn_{1-x}S$ nanowire arrays and found that the incorporation of Zn into CdS significantly increased the resistivity of the nanowires arrays, resulting in an increase in the voltage drop along the nanowires, which in turn suppressed the field-emission efficiency.[31] Recently, Fang et al. have investigated the field emission of several ZnS nanostructures[32,33] and developed two alternative methods to dramatically improve the field-emission properties of ZnS nanostructures: the first one is to increase their aspect ratios through making ZnS ultrafine nanobelts with narrow size distribution; the second one is to fabricate crystal orientation-ordered ZnS nanobelt quasi-arrays using a noncatalytic and template-free thermal evaporation process.[34] To better understand the effects of size and arrangement of nanostructures on their field-emission performances, the influence of various geometries and synthetic conditions has to be ruled out. To the best of our knowledge, the relationships between structure morphologies prepared in analogous conditions with their stimulated and field-emission properties have not yet been systematically investigated.

In this work, we present a simple two-step metal-organic chemical vapor deposition (MOCVD) approach to synthesize high-quality, uniform, and well-aligned CdS 1D nanostructures with different morphologies, such as truncated nanocone arrays, nanorods, cleft nanorod arrays, and nanowire arrays. The morphology of the CdS nanostructures was precisely adjusted by tuning a distance between the precursors and a substrate. Our results demonstrate that the better the alignment, the lower the threshold for a stimulated emission, whereas both the alignments and aspect ratios have greatly influenced the field-emission properties: the CdS emitters with higher aspect ratio and better alignments exhibited better field-emission performance. Thus the well-aligned CdS nanorod arrays have the lower threshold for the stimulated emission, and the quasi-aligned nanowire arrays possess the higher field-emission currents and the lower turn-on fields.

RESULTS AND DISCUSSION

The representative morphologies and structures of the produced CdS nanostructures were investigated by field-emission scanning electron microscopy (FESEM), as shown in Figure 1. The low-magnification SEM images show that the ordered arrays of CdS nanostructures uniformly and compactly cover the entire substrates. The high-magnification SEM images illustrate that the morphologies and alignments of nanostructure arrays are quite different for different distances between the precursors and a substrate. At a short distance, the well-aligned truncated nanocone arrays with coalescent ends are formed. The nanocones have a tip width of 100−200 nm, a bottom width of

200−300 nm, and a length of several micrometers (Figure 1a$_2$). The CdS nanocones are parallel to each other and grow vertically on the substrate with a strong preference to be oriented. On increasing the distance, well-organized, very short, thin, and faceted nanorod arrays grow (Figure 1b$_2$). The tips of the nanorods have an average diameter of 20−50 nm, and the bottoms are 200−300 nm in diameter. The length of the top nanorods may increase, as shown in Figure 1c$_2$ (sample c, well-aligned cleft nanorod arrays), or decrease, and the alignment deteriorates partly, as shown in Figure 1d$_2$ (sample d), under a further increase in distance. The nanowires with a diameter of 30 nm and a length of several micrometers are obtained within quasi-aligned nanowire arrays (sample d). Finally, the alignment of the nanowires with the similar dimensions to sample d has almost vanished when a distance between the precursor and substrate becomes long enough (Figure 1e$_2$). What should be mentioned is that the temperatures of the different zones are almost the same. The distances between the substrates and precursors certainly play an important role in determining the deposit morphology, which in turn leads to dramatic differences in stimulated emission and field-emission performance, as discussed later.

The detailed microstructures of ordered CdS nanostructures were further studied by transmission electron microscopy (TEM). Figure 2a,b shows the typical TEM images of truncated nanocones and cleft nanorods, respectively. It is noteworthy that the upper and lower diameters of the truncated nanocones are 180 and 250 nm, which is consistent with the SEM observations. The upper nanorods of the cleft nanorod are parallel to each other, providing good configuration for the further applications. As can be derived from the electron diffraction (ED) (inset of Figure 2a) and HR-TEM image (Figure 2c), both truncated nanocones and cleft nanorods are single crystals grown along the [001] direction. Figure 2d shows that the quasi-aligned nanowire arrays retain the wirelike array geometry even if they have been scraped off from the substrate and subjected to ultrasonic treatment for 20 min. The enlarged TEM image (Figure 2e) shows that a diameter of the nanowires is ∼30 nm. Figure 2f corresponds to the HRTEM image and shows perfect wurtzite structure with the [100] zone axis, with the corresponding ED displayed in the inset. The fringe spacings shown in the image are ∼0.67 and ∼0.37 nm, in a good agreement with the d spacing of (001) and (010) planes of hexagonal CdS. The axis of the nanowire is parallel to the [001] direction, indicating that the nanowires have been grown along this direction. The highly symmetrical dif-
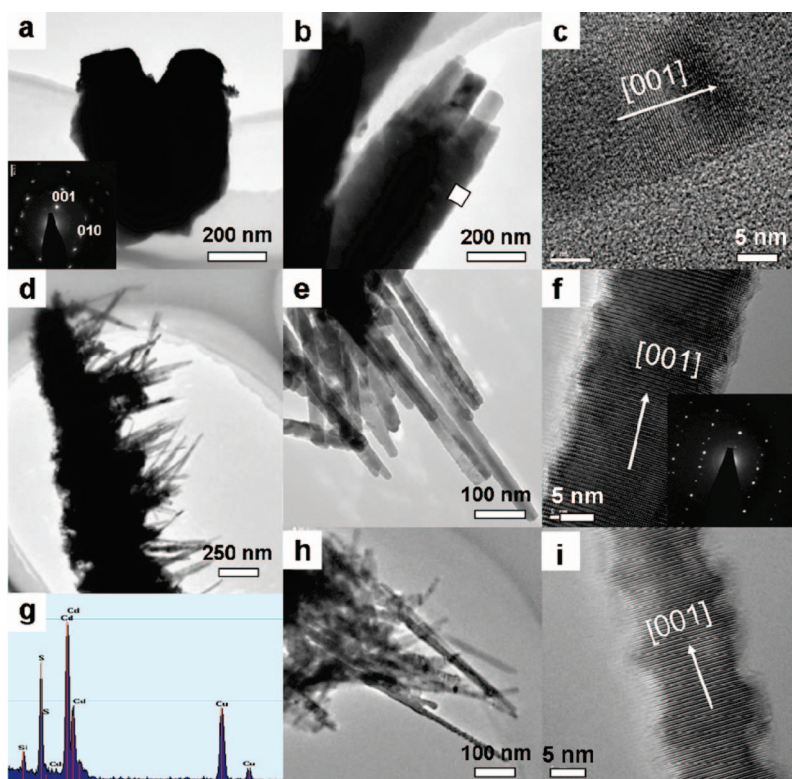

Figure 2. TEM images of various CdS nanostructures. (a) TEM image and ED pattern (inset) of the truncated nanocones (sample a); (b,c) TEM image and HRTEM image of the cleft nanorods (sample c); (d−g) TEM images, HRTEM image, and EDS spectrum of quasi-aligned nanowire arrays (sample d); (h,i) TEM image and HRTEM image of the nanowire arrays (sample e).

fraction pattern and clear lattice fringes indicate that the nanowires are well-crystallized. The energy dispersive X-ray spectrum (EDS) exhibits strong Cd and S peaks, and the atomic ratio of Cd and S is close to the 1:1 stoichiometry, as expected. Figure 2h,i shows the TEM and HRTEM images of the nanowire arrays, which reveal that they are perfectly structured and the growth directions are the same, that is, along the [001] orientation.

The X-ray diffraction (XRD) pattern of the CdS nanostructures (sample a) is shown in Figure 3a. All of the diffraction peaks can be readily indexed to a hexagonal wurtzite-structured CdS with the lattice parameters of $a = 4.14$ Å and $c = 6.72$ Å, in a good agreement with the literature values (JCPDS Card, No. 41-1049). No characteristic peaks of other impurities are detected in this pattern. The sharp diffraction peaks indicate the good crystallinity. Meanwhile, it is noted that the relative intensities of the peaks differ from the standard pattern of a bulk material, which should be caused by preferred orientation and distribution of CdS nanorods. A pattern taken from nanorods shows a strong {002} diffraction peak, which might be due to the growth of wurtzite-structured CdS along the [001] direction, in accord with the HRTEM results. Raman scattering spectroscopy was employed to further study the nanostructures. Figure 3b depicts a room-temperature micro-Raman spectrum
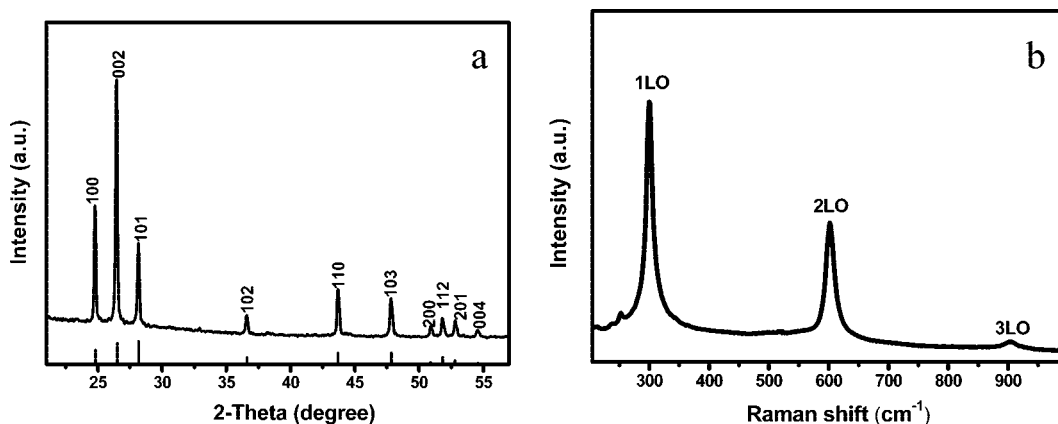
Figure 3. (a) XRD pattern of the as-prepared CdS nanostructures (sample a). The vertical lines at the bottom correspond to the standard XRD pattern of wurtzite CdS (JCPDS No. 41-1049). (b) Micro-Raman spectrum of the CdS nanostructures (sample a) at room temperature.

of the CdS nanostructures (sample a). The hexagonal wurtzite-structured CdS belongs to $C_{6v}^4(P6_3mc)$ space group and may have the following normal lattice vibration modes: $\Gamma_{opt} = A_1 + 2B_1 + E_1 + 2E_2$.[35,36] The A_1, E_1, and E_2 are Raman active, whereas B_1 is forbidden. The weak peaks at 239 and 253 cm^{-1} are ascribed to multiphonon scattering, A_1(TO) and E_2^H, which have

been reported in CdS nanowires.[37] Three strong peaks located around 300, 602, and 902 cm^{-1} can be assigned to the first-, second-, and third-order longitudinal optical (LO) phonon modes of CdS,[38−41] respectively. The relatively broad, symmetric, and sharp peaks of CdS nanostructures suggest that the nanorods are highly crystalline, which is 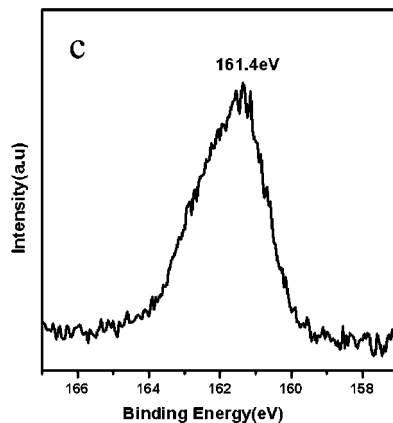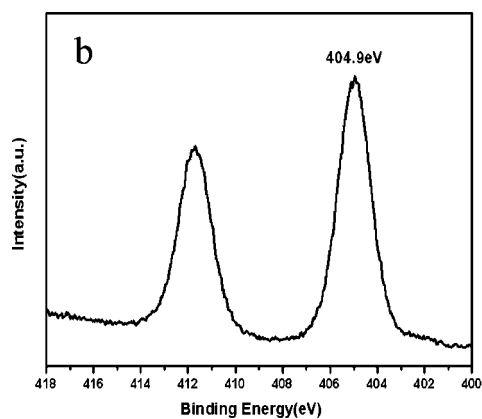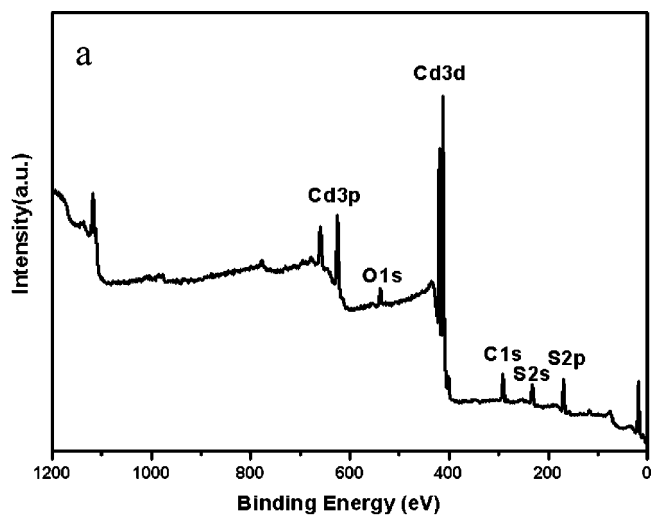consistent with the XRD patterns and the HRTEM observations shown above. Further evidence of the high crystal quality was obtained using X-ray photoelectron spectroscopy (XPS). Figure 4a shows the survey spectrum of CdS truncated nanocone arrays (sample a), and no peaks of other elements except Cd, S, C, and O are observed. The C and O peaks come mainly from the atmospheric contamination due to a sample exposure to air. The binding energies obtained in the XPS analysis were corrected taking into account the specimen charging and by referring to C 1s at 284.60 eV. The Cd 3d5 and S 2p features, shown in Figure 4b,c, have binding energies of E_B = 404.9 and 161.4 eV, respectively. These results agree well with those reported previously.[42]

For the growth of nanostructures in a vapor deposition system, two growth mechanisms have been proposed, namely, the vapor−solid (VS)[43] and vapor−liquid−solid (VLS).[44,45] The VLS mechanism can be ruled out here because no metal particles have been found on the tips of the CdS nanostructures (which is a finger-

Figure 4. XPS analysis of the as-prepared CdS nanostructures (sample a): (a) survey spectrum; (b) Cd-3d binding energy spectrum; (c) S-2p binding energy spectrum.
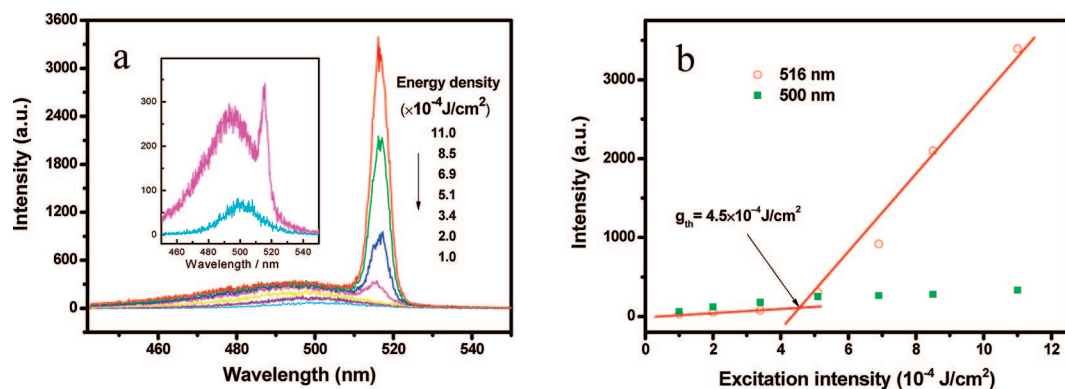
Figure 5. (a) Power-dependent PL spectra of the CdS nanowire arrays (sample d) excited by femtosecond laser pulses with various excitation power densities at room temperature. The inset is the enlargement of the two curves at 1.0×10^{-4} and 5.1×10^{-4} J/cm^2. **(b)** Excitation power dependence of the emission intensity for spectra positions at 500 and 516 nm.

print of the VLS model). Thus we suggest that the VS mechanism is dominant. Initially, the $Cd(S_2CNEt_2)_2$ vapor generated by thermal evaporation is transported by the carrier gas to the substrates located at the high-temperature zone and then decomposed to form CdS vapor. It is obvious that the CdS vapor supersaturation plays an important role: the growth of nanocones, nanorods, cleft nanorods, and nanowires can be controlled by adjusting a distance between the precursors and a substrate. From the viewpoint of the system Helmholtz free energy minimum, when the crystalline facets are the same for different nanostructures, a lower pressure would facilitate a higher surface-to-volume ratio.[46,47] The formation of truncated nanocones with coalescent ends can be attributed to a sum effect of the 3D and anisotropic growth rates. Due to the large difference in surface free energy between CdS and a substrate, the CdS deposits grow in the 3D island mode, and then these islands grow larger and meet to form a CdS film. Such a scenario has commonly been observed in the literature.[48] The decrease of the CdS vapor pressure with the consumption of the precursor favors the high surface-to-volume ratio growth mode, enabling a transformation from a film to nanorod growth (the structure diameter decreases), which results in the formation of the truncated nanocones. As a typical wurtzite crystal, CdS is intrinsically an anisotropic material with the specific c-axis. A hexagonal CdS crystal can be described as a stacking of the {CdS4} tetrahedrons sharing the common corners. Each tetrahedron has a corner in the [001] direction.[49] The atom at the corner of a tetrahedron has the strong bonding force ($s = 2$ v.u.), compared with the atoms at other positions,[50,51] which favors the growth of CdS nanocones along the [001] axis. With increasing distance between the substrates and the precursors, the degree of supersaturation and diffusion rate of CdS molecules decrease accordingly, resulting in the formation of cleft nanorods and nanowires with a higher surface-to-volume ratio. On the other hand, the vapor pressure fluctuations during the

reaction become more prominent due to a decreased distance to the pump, which results in the poor alignment of the nanostructures.

The uniform dimensions and good crystallinities of the obtained CdS nanostructure arrays indicate that the stimulated emission or lasing under high excitation may be realized in them. Figure 5a shows the power-dependent photoluminescence (PL) spectra of CdS nanorods (sample d) excited by the femtosecond laser pulses with various power densities at room temperature. The laser was incident to the sample at an angle of 45°, and the acquisition direction was perpendicular to the sample, as shown in Figure S1 in Supporting Information. At a low excitation intensity, a broad and weak band appears at 500.1 nm (2.480 eV), which is attributed to the spontaneous exciton transition at the CdS band gap.[22] When the excitation power density increases to ~5.1×10^{-4} J/cm^2, a new sideband appears at 515.6 nm (2.405 eV), at the low energy side of the broad mainband. This sideband with a ~75 meV red shift is attributed to the E-2LO phonon band since 2LO phonon energy (*ca.* 76 meV) is close to the observed red shift and larger than the available thermal energy at room temperature (~26 meV). This peak has a full width at half-maximum (fwhm) of 5 nm, which is less than for spontaneous exciton emission, and its output intensity increases rapidly, clearly indicating a lasing action. For bulk and nanoscale CdS, three mechanisms are known to produce significant gain: exciton–exciton (E–E) scattering, exciton–longitudinal optic (ex–LO) phonon scattering, and electron–hole plasma (EHP).[52] The formation of EHP is generally accompanied with a strong red shift and the spectrum broadening due to the band gap renormalization effect.[53] The absence of a red shift and broadening with increasing excitation intensity rules out the EHP mechanism. In addition, for exciton–exciton scattering, the peak position for exciton–exciton collision (during which one of the excitons was scattered to the *n*th exciton level) is given by[54,55]

$$p_n = E_{ex} - E_b^{ex}\left(1 - \frac{1}{n^2}\right) - \frac{3}{2}kT \qquad (1)$$
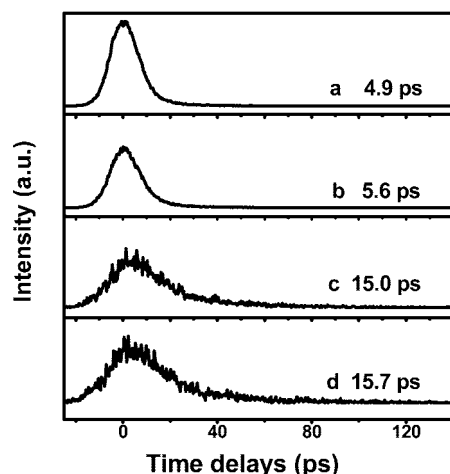
Figure 6. (a) PL lifetime decay profiles of CdS nanowire arrays (sample d) at different pumping energies: (a) 11×10^{-4} J/cm^2; (b) 5.1×10^{-4} J/cm^2; (c) 3.4×10^{-4} J/cm^2; (d) 1.0×10^{-4} J/cm^2. The curves are well-fitted by a single-exponential function.

where p_n is the phonon energy, E_{ex} is the free-exciton emission energy, E_b^{ex} is the binding energy of an exciton (29.4 meV for CdS[56]), n is the quantum number of the envelope function, and kT is the thermal energy. Equation 1 gives an energy difference between the free-exciton peak and the exciton−exciton of 61 meV ($n = 2$), which is much smaller than the experimental energy shift (75 meV). These results further prove lasing by the ex−LO mechanism in the range of the excitation intensities used in our study.

Figure 5bplots the excitation power dependence of the emission intensity for spectral positions at 500 and 516 nm. It clearly shows that the PL intensity at 500 nm has an approximately linear increase with rising of the excitation power, whereas the emission intensity at 516 nm has a supralinear dependence on the excitation power, with a threshold at 4.5×10^{-4} J/cm^2. The supralinear increase in emission intensity is a characteristic of the amplified stimulated emission and lasing. These spectral characteristics were further studied by the PL decay profiles as a function of pumping energy. The PL

lifetime is also very important for luminescent semiconductor nanostructures in various applications, such as LEDs, biological labeling, solar cells, lasers, and so forth.[57] Figure 6 displays the room-temperature decay curves of CdS nanowire arrays at different excitation intensities from 1.0×10^{-4} to 11×10^{-4} J/cm^2. All these curves can be well-fitted by a single-exponential function. At the low excitation intensities, the PL lifetime of spontaneous emission is ~15.7 ps, and its lifetime slightly decreases with an increase in pumping energy. Under further power increase to 5.1×10^{-4} J/cm^2, above the threshold (4.5×10^{-4} J/cm^2), the lifetime decreases rapidly from 15.7 to 5.6 ps. The obviously shortened PL lifetimes indicate that the confined PL is under a resonance under high excitation, which further confirms the occurrence of stimulated emissions in these CdS nanowire arrays.[58]

Figure 7a shows the lasing threshold of the as-prepared CdS nanostructures. It is clear that the well-aligned nanorod arrays (sample b) have the lower threshold (0.8×10^{-4} J/cm^2), compared to the well-aligned truncated nanocone arrays (1.2×10^{-4} J/cm^2), well-aligned cleft nanorod arrays (1.0×10^{-4} J/cm^2), and quasi-aligned nanowire arrays (4.5×10^{-4} J/cm^2). We do not observe the stimulated emission phenomenon in the nanowire arrays (sample e). Figure 7b presents the room-temperature PL spectra of CdS nanowire arrays (sample e). The PL spectra of the arrays display a broad and weak band around 500.8 nm, which is attributed to the spontaneous exciton transition at the CdS band gap, as discussed before. With the rise of the excitation power density, the intensities of the spontaneous emission are enhanced, and the peak position blue shifts from 500.8 to 495.3 nm. Even if the excitation power density increases above 1.5×10^{-3} J/cm^2, no peak around 516 nm attributed to stimulated emission can be observed. The lasing threshold is dependent upon the nature of the nanostructures, such as dimensions, alignment, ending facets, and crystal quality, as well as substrate coupling.[59] We suggest that the lasing threshold is mainly dependent on the orientation of an array. Samples a, b, and c have the similar orientations, which result in the similar lower thresholds. Sample d has the poorest orientation, leading to the higher threshold. When the alignment deteriorates, no stimulated emission is observed.

Field-emission (FE) measurements show that the CdS nanostructures are potentially good field emitters. Until now, the studies on the field-emission (FE) properties of CdS nanostructures have been rather limited compared to other field emitters such as carbon nanotubes and ZnO and ZnS nanomaterials.[33] The field emission from the present CdS nano-
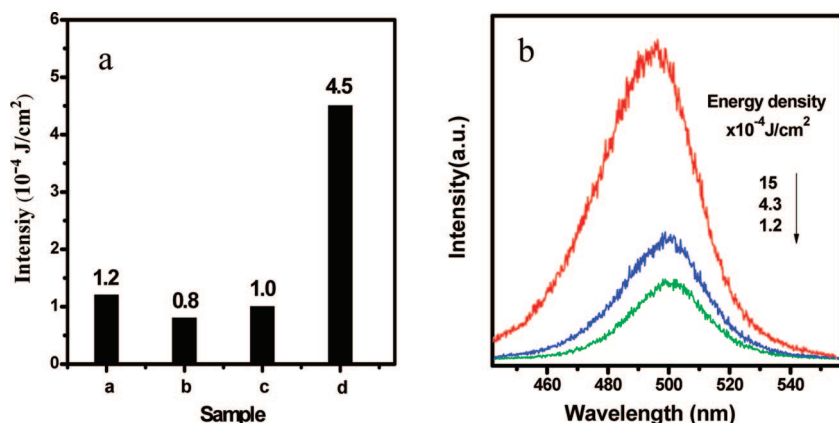

Figure 7. (a) Threshold for lasing of the as-prepared CdS nanostructures (samples a−d). (b) Power-dependent PL spectra of the CdS nanowire arrays (sample e) excited by femtosecond laser pulses with various excitation power densities at room temperature.
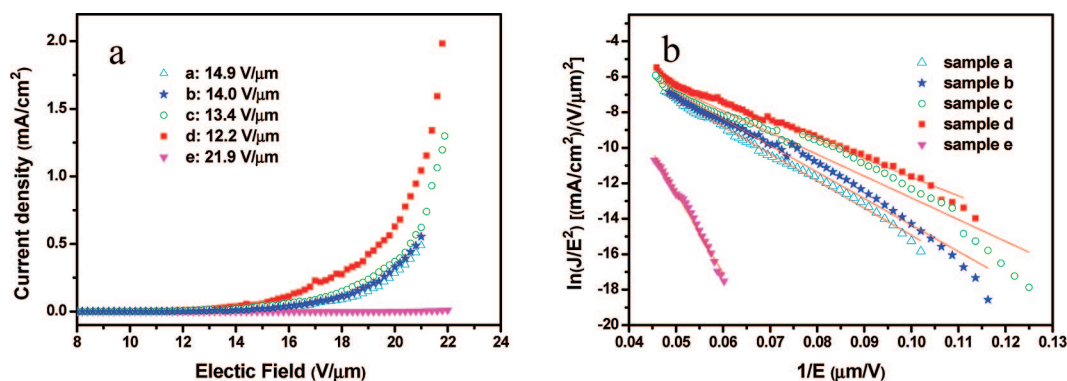
Figure 8. Field-emission properties of the as-grown CdS nanostructures. (a) FE current density *versus* the applied field (J−E) curves from the five samples at a working distance of 50 μm; (b) corresponding Fowler−Nordheim (FN) plots roughly showing linear dependence.

structures was measured at a 50 μm gap between the anode and a sample in a vacuum chamber maintained at a pressure of 1.6×10^{-6} Pa. The curves of the emission current density *versus* the applied field curve (J−E) from the five samples are shown in Figure 8a. The quasi-aligned nanowire arrays (sample d) have the best field-emission properties with the lowest turn-on field (E_{to}, defined as E at which J becomes 10 μA/cm^2) of 12.2 V/μm, the lowest threshold field (defined as E at which J becomes 0.1 mA/cm^2) of 15.7 V/μm, and the highest J at the same E value. The FE current density reaches 2.0 mA/cm^2 (the total current reaches 2.0×10^{-5} A) when an applied macroscopic field is 21.8 V/μm. Meanwhile, the turn-on fields from the other samples are 14.9, 14.0, 13.4, and 21.9 V/μm, as shown in Table 1. It is noted that the threshold field from nanowire arrays (sample e) could not be measured due to a very small current density (far below 0.1 mA/cm^2) in the available voltage range. In comparison to the FE characteristics of CdS nanowire arrays reported by other researchers,[60] the E_{to} value of sample d is lower, but the value of the sample e is higher. This discrepancy may be due to a smaller number of the present emitter tips that resulted from the coalescence of nanowires, as indicated in Figure 1 and in ref 60.

The FE current−voltage characteristics are further analyzed by the Fowler−Nordheim (F−N) equation[61,62]

$$J = (A\beta^2 E^2/\varphi)\exp(-B\varphi^{3/2}\beta E) \qquad (2)$$

or

$$\ln(J/E^2) = \ln(A\beta^2/\varphi) - B\varphi^{3/2}/\beta E \qquad (3)$$

where A and B are constants with values of 1.54×10^{-6} A eV V^{-2} and 6.83×10^3 V μm^{-1} eV$^{-3/2}$, respectively, J is the current density, β is the field-enhancement factor, E is the applied field, and Φ is the work function of the emitting materials, which is 4.2 eV for CdS. Generally, the values of β are related to the emitter geometry (such as aspect ratios), crystal structure, vacuum gaps, and the spatial distribution of emitting centers.[63] The linear variation of $\ln(J/E^2)$ with $(1/E)$

(F−N plot) (Figure 7b) implies that the electron emission from CdS nanorod arrays follows the F−N behavior. The calculated field-enhancement factors from the F−N plots are also summarized in Table 1. Quasi-aligned nanowire arrays (sample d) have the highest β value (555) compared to sample a (384), sample b (408), sample c (450), and sample e (129). The excellent field-emission properties and high β of sample d are likely attributed to the higher aspect ratio (or smaller emitter radius) than those of samples a, b, and c and the better alignment (see Figure 1) than that of sample e.

Figure 9a illustrates a F−E curve for the well-aligned CdS truncated nanocone arrays (sample a) measured at different vacuum gaps (d). When a vacuum gap increases from 30 to 70 μm, the turn-on field decreases monotonously from 23.8 to 11.5 V/μm during a voltage increase. Meanwhile, the threshold field also decreases from 28.4 to 14.9 V/μm. From the slope of the linear part of the F−N plot, β can be calculated to be 261, 348, 373, 505, and 602 for d = 30, 40, 50, 60, and 70 μm, respectively. The $1/\beta$ *versus* $1/d$ plot is given in Figure 9c. This allows us to establish the relationship between β and d. It is clear that $1/\beta$ follows the trend for $1/d$, that is, the larger a vacuum gap, the higher the β. On the basis of the two-region field-emission (TRFE) model,[64] we found that the experimental data are almost perfectly fitted to a straight line and can be approximated by $1/\beta = h/d + 1/\beta_0$, where h is the width of the field-enhancement region near the nanorod surface and β_0 is the absolute amplification factor, which is intrinsically determined by emitters and independent of d and an applied field. The h and β_0 (determined by fitting the

TABLE 1. Turn-On and Threshold Fields and β for the Prepared CdS Nanostructure Arrays

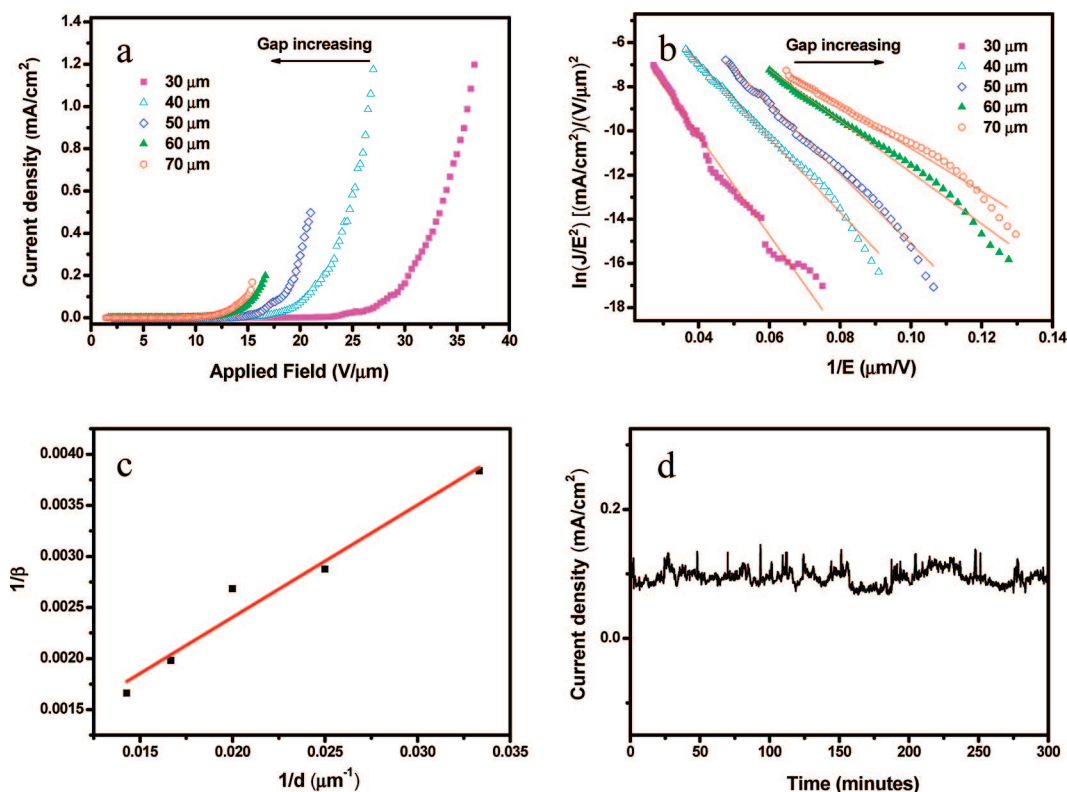| samples	morphology	turn-on field (V/μm)	threshold field (V/μm)	β
a	well-aligned truncated nanocone arrays	14.9	18.3	384
b	well-aligned nanorod arrays	14.0	17.8	408
c	well-aligned cleft nanorod arrays	13.4	17.2	450
d	quasi-aligned nanowire arrays	12.2	15.7	555
e	nanowire arrays	21.9		129

Figure 9. (a) *J−E* plots and (b) corresponding F−N plots from well-aligned truncated nanocone arrays (sample a) with different vacuum gaps; (c) relationship between the field-enhancement factor β and a vacuum gap *d*. The straight line is the linear fit to experimental data based on the TRFE model; (d) the field-emission stability data over ∼5 h acquired at the emission current density of 0.1 mA/cm².

slope and intercept value) are ∼110 nm and ∼4933, respectively. The value of β_0 revealed by the present nanocone arrays is comparable to that of the carbon nanotubes grown on a Si wafer ($\beta_0 = 7900$)[64] and that of ZnO nanorods grown on a Si substrate ($\beta_0 = 3738$),[65] and much larger than that of an Al-doped ZnO emitter ($\beta_0 = 1845$).[66] However, *h* is much smaller than the values reported in the literature (*h* is 540 nm for CNT grown on a Si wafer[64]), which is probably due to the strong screening effect caused by the higher density and coalescent ends of the nanocones.

Stability of the field emitters is another important parameter related to potential applications. FE stability measurements were performed on the well-aligned truncated nanocone arrays (sample a) by keeping an electric field at 20 V/μm over a period of 5 h. As shown in Figure 9d, there were not any current degradations or notable fluctuations during this period. Good emission stability demonstrates that the CdS nanostructures could find potential applications in the cold-cathode-based electronics.

CONCLUSIONS

In summary, ordered CdS nanostructure arrays with different morphologies were fabricated through a two-step metal-organic chemical vapor deposition method. Through increasing the distances between precursors and substrates, the morphology of CdS nanostructure arrays was varied from truncated nanocones, nanorods, or cleft nanorods to nanowires arrays. Although the detailed mechanism requires further investigations, the present results suggest that this simple method might be useful for the synthesis of other semiconductor nanostructures to meet the growing demands of the nanotechnology. The stimulated emission and field emission of the five ordered CdS nanostructure arrays with different morphologies were thoroughly investigated. Generally, different 1D CdS nanostructure arrays have obvious differences in stimulated and field emission. The alignments of CdS nanostructures have a prime effect on their stimulated emission properties, the better the alignments, the lower the threshold, but the dimensions (or aspect ratio) have a little effect on their stimulated emission properties, while both the alignments and aspect ratios have a significant influence on their field-emission properties. The CdS emitters with a higher aspect ratio and better alignment exhibited better field-emission performance. Well-aligned CdS nanorod arrays have the lower threshold for the stimulated emission, whereas quasi-aligned nanowire arrays produce the higher field-emission current and possess the lower turn-on field owing to the higher aspect ratio and better alignment. We envisage that the present CdS nanostructure arrays are promising candidates for future applications in flat panel displays, high brightness electron sources, and nanolasers.

METHODS

The CdS nanorod arrays were synthesized through a low-pressure thermal decomposition process described previously,[67−69] as shown in Figure S2 in Supporting Information. In short, homemade $Cd(S_2CNEt_2)_2$ powders were put in a quartz boat at the upstream end of the tube furnace. Several p-type Si substrates covered with Au nanocrystals were placed on the high-temperature zone to collect the products, and the distances between the substrates and left margin of the furnace were ~16, 18, 23, 25, and 27 cm for samples a−e, respectively. First, the furnace was rapidly heated to 650 °C and maintained for 120 min and then cooled to room temperature. Second, the quartz boat was taken out of the furnace and filled with the $Cd(S_2CNEt_2)_2$ powders again and placed back into the furnace. The furnace was heated to 420 °C and held at that temperature for 240 min. All of the growths were carried out under a N_2 flow of 60 sccm at a base pressure of 100 Pa. After that, the furnace was cooled to room temperature slowly. The nanomaterials were collected on the Si wafers at different positions in the furnace.

The synthesized products were characterized by a scanning electron microscope (SEM, Hitachi F-4300) with an X-ray energy dispersed spectrometer (EDS), X-ray diffraction (XRD, Rigaku D/max-2400PC) with Cu Kα radiation, a transmission electron microscope (TEM, JEOL JEM-1011), and a high-resolution TEM (HRTEM, Philips Tecnai F30). X-ray photoelectron spectra were measured using an ESCALab220i-XL electron spectrometer from VG Scientific using 300 W Al Kα radiations. The binding energies were referenced to the C 1s line at 284.6 eV of carbon. The Raman spectra were recorded in the backscattering geometry by using a Renishaw-2000 Raman spectrometer with a 514.5 nm line of an Ar ion laser as the excitation source. Photoluminescence (PL) measurements were optically pumped by the third harmonic of a mode-locked Ti:sapphire laser (266 nm in wavelength, 150 fs pulse width). The pump laser shone the CdS nanostructures at an incidence angle of 45°, and the light emission was collected along the sample surface normal direction. The PL detector was a streak camera (C5680, Hamamatsu Photonics) attached to a polychromator (C5094, Hamamatsu Photonics). The temporal and spectral resolutions of the detector were ~2 ps and ~0.2 nm, respectively. The field-emission properties were studied at room temperature in a high vacuum chamber (1.6 × 10^{-6} Pa) using a 1 mm^2 cross-sectional area aluminum anode. A dc voltage sweeping from 100 to 1100 V was applied to the samples.

Supporting Information Available: Setup of PL experiments and schematic illustration of the apparatus. This material is available free of charge *via* the Internet at http://pubs.acs.org.

REFERENCES AND NOTES

1. Rao, C. N. R.; Govindaraj, A. *Nanotubes and Nanowires*, RSC Nanoscience & Nanotechnology Series; RSC Publishing: Cambridge, UK, 2005.
2. Zeng, H. B.; Cai, W. P.; Liu, P. S.; Xu, X. X.; Zhou, H. J.; Kingshirn, C.; Kalt, H. ZnO-Based Hollow Nanoparticles by Selective Etching: Elimination and Reconstruction of Metal/Semiconductor Interface, Improvement of Blue Emission and Photocatalysis. *ACS Nano* **2008**, *2*, 1661–1670.
3. Bai, X. D.; Wang, E. G.; Gao, P. X.; Wang, Z. L. Measuring the Work Function at a Nanobelt Tip and at a Nanoparticle Surface. *Nano Lett.* **2003**, *3*, 1147–1150.
4. Wang, X. D.; Zhou, J.; Lao, C. S.; Song, J. H.; Xu, N. S.; Wang, Z. L. *In Situ* Field Emission of Density-Controlled ZnO Nanowire Arrays. *Adv. Mater.* **2007**, *19*, 1627–1631.
5. Law, M.; Greene, L. E.; Johnson, J. C.; Saykally, R.; Yang, P. D. Nanowire Dye-Sensitized Solar Cells. *Nat. Mater.* **2005**, *4*, 455–459.
6. Huang, M. H.; Mao, S.; Feick, H.; Yan, H. Q.; Wu, Y. Y.; Kind, H.; Weber, E.; Russo, R.; Yang, P. D. Room-Temperature Ultraviolet Nanowire Nanolasers. *Science* **2001**, *292*, 1897–1899.
7. Jiang, Y.; Zhang, W. J.; Jie, J. S.; Meng, X. M.; Zapien, J. A.; Lee, S. T. Homoepitaxial Growth and Lasing Properties of ZnS Nanowire and Nanoribbon Arrays. *Adv. Mater.* **2006**, *18*, 1527–1532.
8. Yuan, G. D.; Zhang, W. J.; Jie, J. S.; Fan, X.; Zapien, J. A.; Leung, Y. H.; Luo, L. B.; Wang, P. F.; Lee, C. S.; Lee, S. T. p-Type ZnO Nanowire Arrays. *Nano Lett.* **2008**, *8*, 2591–2597.
9. Ito, D.; Jespersen, M. L.; Hutchison, J. E. Selective Growth of Vertical ZnO Nanowire Arrays Using Chemically Anchored Gold Nanoparticles. *ACS Nano* **2008**, *2*, 2001–2006.
10. Wang, Z. L.; Song, J. H. Piezoelectric Nanogenerators Based on Zinc Oxide Nanowire Arrays. *Science* **2006**, *312*, 242–246.
11. Wang, X. D.; Song, J. H.; Liu, J.; Wang, Z. L. Direct-Current Nanogenerator Driven by Ultrasonic Waves. *Science* **2007**, *316*, 102–105.
12. Adhikari, H.; Marshall, A. F.; Chidsey, C. E. D.; McIntyre, P. C. Germanium Nanowire Epitaxy: Shape and Orientation Control. *Nano Lett.* **2006**, *6*, 318–323.
13. Duan, X. F.; Lieber, C. M. General Synthesis of Compound Semiconductor Nanowires. *Adv. Mater.* **2000**, *12*, 298–302.
14. Xu, S.; Wei, Y. G.; Kirkham, M.; Liu, J.; Mai, W. J.; Davidovic, D.; Snyder, R. L.; Wang, Z. L. Patterned Growth of Vertically Aligned ZnO Nanowire Arrays on Inorganic Substrates at Low Temperature without Catalyst. *J. Am. Chem. Soc.* **2008**, *130*, 14958–14959.
15. Gao, P. X.; Ding, Y.; Wang, Z. L. Crystallographic Orientation-Aligned ZnO Nanorods Growth by a Tin Catalyst. *Nano Lett.* **2003**, *3*, 1315–1320.
16. Mai, W. J.; Gao, P. X.; Lao, C. S.; Wang, Z. L.; Sood, A. K.; Polla, D. L.; Soprano, M. B. Vertically Aligned ZnO Nanowire Arrays on GaN and SiC Substrates. *Chem. Phys. Lett.* **2008**, *460*, 253–256.
17. Pan, H.; Poh, C. K.; Zhu, Y. W.; Xing, G. C.; Chin, K. C.; Feng, Y. P.; Lin, J. Y.; Sow, C. H.; Ji, W.; Wee, A. T. S. Novel CdS Nanostructures: Synthesis and Field Emission. *J. Phys. Chem. C* **2008**, *112*, 11227–11230.
18. Lin, Y. F.; Song, J. H.; Ding, Y.; Lu, S. Y.; Wang, Z. L. Alternating the Output of a CdS Nanowire Nanogenerator by a White-Light-Stimulated Optoelectronic Effect. *Adv. Mater.* **2008**, *20*, 3127–3130.
19. Shen, G. Z.; Cho, J. H.; Yoo, J. K.; Yi, G. C.; Lee, C. J. Synthesis of Single-Crystal CdS Microbelts Using a Modified Thermal Evaporation Method and Their Photoluminescence. *J. Phys. Chem. B* **2005**, *109*, 9294–9298.
20. Duan, X. F.; Huang, Y.; Agarwal, R.; Lieber, C. M. Single-Nanowire Electrically Driven Lasers. *Nature* **2003**, *421*, 241–245.
21. Pan, A. L.; Liu, D.; Liu, R. B.; Wang, F. F.; Zhu, X.; Zou, B. S. Optical Waveguide through CdS Nanoribbons. *Small* **2005**, *1*, 980–983.
22. Pan, A. L.; Liu, R. B.; Yang, Q.; Zhu, Y. C.; Yang, G. Z.; Zou, B. S.; Chen, K. Q. Stimulated Emissions in Aligned CdS Nanowires at Room Temperature. *J. Phys. Chem. B* **2005**, *109*, 24268–24272.
23. Kar, S.; Chaudhuri, S. Shape Selective Growth of CdS One-Dimensional Nanostructures by a Thermal Evaporation Process. *J. Phys. Chem. B* **2006**, *110*, 4542–4547.
24. Gao, H. Q.; Xu, Y.; Hong, J. M.; Liu, H. B.; Yin, G.; Li, B. L.; Tie, C. Y.; Xu, Z. Sol−Gel Template Synthesis of an Array of Single Crystal CdS Nanowires on a Porous Alumina Template. *Adv. Mater.* **2001**, *13*, 1393–1394.

25. Cao, B. L.; Jiang, Y.; Wang, C.; Wang, W. H.; Wang, L. Z.; Niu, M.; Zhang, W. J.; Li, Y. Q.; Lee, S. T. Synthesis and Lasing Properties of Highly Ordered CdS Nanowire Arrays. *Adv. Funct. Mater.* **2007**, *17*, 1501–1506.

26. Hsu, Y. J.; Lu, S. Y. Dopant-Induced Formation of Branched CdS Nanocrystals. *Small* **2008**, *4*, 951–955.

27. Shen, G. Z; Bando, Y.; Liu, B. D.; Golberg, D.; Lee, C. J. Characterization and Field-Emission Properties of Vertically Aligned ZnO Nanonails and Nanopencils Fabricated by a Modified Thermal-Evaporation Process. *Adv. Funct. Mater.* **2006**, *16*, 410–416.

28. Ye, C. H; Bando, Y.; Fang, X. S.; Shen, G. Z.; Golberg, D. Enhanced Field Emission Performance of ZnO Nanorods by Two Alternative Approaches. *J. Phys. Chem. C* **2007**, *111*, 12673–12676.

29. Fang, X. S.; Bando, Y.; Gautam, U. K.; Ye, C. H.; Golberg, D. Inorganic Semiconductor Nanostructures and Their Field-Emission Applications. *J. Mater. Chem.* **2008**, *18*, 509–522.

30. Zhao, Q.; Zhang, H. Z.; Zhu, Y. W.; Fang, S. Q.; Sun, X. C.; Xu, J.; Yu, D. P. Morphological Effects on the Field Emission of ZnO Nanorod Arrays. *Appl. Phys. Lett.* **2005**, *86*, 203115.

31. Lin, Y. F.; Hsu, Y. J.; Lu, S. Y.; Chen, K. T.; Tseng, T. Y. Well-Aligned Ternary $Cd_{1-x}Zn_xS$ Nanowire Arrays and Their Composition-Dependent Field Emission Properties. *J. Phys. Chem. C* **2007**, *111*, 13418–13426.

32. Fang, X. S.; Bando, Y.; Ye, C. H.; Golberg, D. Crystal Orientation-Ordered ZnS Nanobelt Quasi-Arrays and Their Enhanced Field-Emission. *Chem. Commun.* **2007**, 3048–3050.

33. Fang, X. S.; Bando, Y.; Shen, G. Z.; Ye, C. H.; Gautam, U. K.; Costa, P. M. F. J.; Zhi, C. Y.; Tang, C. C.; Golberg, D. Ultrafine ZnS Nanobelts as Field Emitters. *Adv. Mater.* **2007**, *19*, 2593–2596.

34. Fang, X. S.; Gautam, U. K.; Bando, Y.; Dierre, B.; Sekiguchi, T.; Golberg, D. Multiangular Branched ZnS Nanostructures with Needle-Shaped Tips: Potential Luminescent and Field-Emitter Nanomaterial. *J. Phys. Chem. C* **2008**, *112*, 4735–4742.

35. Pan, H.; Xing, G. C.; Ni, Z. H.; Ji, W.; Feng, Y. P.; Tang, Z.; Chua, D. H. C.; Lin, J. Y.; Shen, Z. X. Stimulated Emission of CdS Nanowires Grown by Thermal Evaporation. *Appl. Phys. Lett.* **2007**, *91*, 193105.

36. Zhai, T. Y.; Gu, Z. J.; Fu, H. B.; Ma, Y.; Yao, J. N. Synthesis of Single-Crystal ZnS Nanoawls *via* Two-Step Pressure-Controlled Vapor-Phase Deposition and Their Optical Properties. *Cryst. Growth Des.* **2007**, *7*, 1388–1392.

37. Fan, H. M.; Fan, X. F.; Ni, Z. H.; Shen, Z. X.; Feng, Y. P.; Zou, B. S. Orientation-Dependent Raman Spectroscopy of Single Wurtzite CdS Nanowires. *J. Phys. Chem. C* **2008**, *112*, 1865–1870.

38. Shen, X. P.; Yuan, A. H.; Wang, F.; Hong, J. M.; Xu, Z. Fabrication of Well-Aligned CdS Nanotubes by CVD-Template Method. *Solid State Commun.* **2005**, *133*, 19–22.

39. Chen, F.; Zhou, R. J.; Yang, L. G.; Liu, N.; Wang, M.; Chen, H. Z. Large-Scale and Shape-Controlled Syntheses of Three-Dimensional CdS Nanocrystals with Flowerlike Structure. *J. Phys. Chem. C* **2008**, *112*, 1001–1007.

40. Wang, Z. Q.; Gong, J. F.; Duan, J. H.; Huang, H. B.; Yang, S. G.; Zhao, X. N.; Zhang, R.; Du, Y. W. Direct Synthesis and Characterization of CdS Nanobelts. *Appl. Phys. Lett.* **2006**, *89*, 033102.

41. Shen, G. Z.; Lee, C. J. CdS Multipod-Based Structures through a Thermal Evaporation Process. *Cryst. Growth Des.* **2005**, *5*, 1085–1089.

42. Zhai, T. Y.; Gu, Z. J.; Yang, W. S.; Zhang, X. Z.; Huang, J.; Zhao, Y. S.; Yu, D. P.; Fu, H. B.; Ma, Y.; Yao, J. N. Fabrication, Structural Characterization and Photoluminescence of Single-Crystal $Zn_xCd_{1-x}S$ Zigzag Nanowires. *Nanotechnology* **2006**, *17*, 4644–4649.

43. Pan, Z. W.; Dai, Z. R.; Wang, Z. L. Nanobelts of Semiconducting Oxides. *Science* **2001**, *291*, 1947–1949.

44. Zhai, T. Y.; Zhong, H. Z.; Gu, Z. J.; Peng, A. D.; Fu, H. B.; Ma, Y.; Li, Y. F.; Yao, J. N. Manipulation of the Morphology of ZnSe Sub-Micron Structures Using CdSe Nanocrystals as the Seeds. *J. Phys. Chem. C* **2007**, *111*, 2980–2986.

45. Zhong, H. Z.; Li, Y. C.; Zhou, Y.; Yang, C. H.; Li, Y. F. Controlled Synthesis of 3D Nanostructured $Cd_4Cl_3(OH)_5$ Templates and Their Transformation into $Cd(OH)_2$ and CdS Nanomaterials. *Nanotechnology* **2006**, *17*, 772–777.

46. Zhang, B. P.; Binh, N. T.; Wakatsuki, K.; Segawa, Y.; Yamada, Y.; Usami, N.; Kawasaki, M.; Koinuma, H. Pressure-Dependent ZnO Nanocrystal Growth in a Chemical Vapor Deposition Process. *J. Phys. Chem. B* **2004**, *108*, 10899–10902.

47. Markov, I. V. *Crystal Growth for Beginners, Fundamentals of Nucleation, Crystal Growth and Epitaxy*; Word Scientific: Singapore, 1996; p, 13.

48. Lin, Y. F.; Hsu, Y. J.; Lu, S. Y.; Kung, S. C. Non-catalytic and Template-Free Growth of Aligned CdS Nanowires Exhibiting High Field Emission Current Densities. *Chem. Commun.* **2006**, 2391–2393.

49. Zhu, Y. C.; Bando, Y.; Xue, D. F.; Golberg, D. Oriented Assemblies of ZnS One-Dimensional Nanostructures. *Adv. Mater.* **2004**, *16*, 831–834.

50. Zhai, T. Y.; Gu, Z. J.; Zhong, H. Z.; Dong, Y.; Ma, Y.; Fu, H. B.; Li, Y. F.; Yao, J. N. Design and Fabrication of Rocketlike Tetrapodal CdS Nanorods by Seed-Epitaxial Metal-Organic Chemical Vapor Deposition. *Cryst. Growth Des.* **2007**, *7*, 488–491.

51. Brown, I. D.; Altermatt, D. Bond-Valence Parameters Obtained from a Systematic Analysis of the Inorganic Crystal Structure Database. *Acta Crystallogr., Sect. B* **1985**, *41*, 244.

52. Agarwal, R.; Barrelet, C. J.; Lieber, C. M. Lasing in Single Cadmium Sulfide Nanowire Optical Cavities. *Nano Lett.* **2005**, *5*, 917–920.

53. Szarko, J. M.; Song, J. K.; Blackledge, C. W.; Swart, I.; Leone, S. R.; Li, S. H.; Zhao, Y. P. Optical Injection Probing of Single ZnO Tetrapod Lasers. *Chem. Phys. Lett.* **2005**, *404*, 171–176.

54. Bagnall, D. M.; Chen, Y. F.; Zhu, Z.; Yao, T.; Koyama, S.; Shen, M. Y.; Goto, T. Optically Pumped Lasing of ZnO at Room Temperature. *Appl. Phys. Lett.* **1997**, *70*, 2230–2232.

55. Djurii, A. B.; Kwok, W. M.; Leung, Y. H.; Phillips, D. L.; Chan, W. K. Stimulated Emission in ZnO Nanostructures: A Time-Resolved Study. *J. Phys. Chem. B* **2005**, *109*, 19228–19233.

56. Jeong, T. S.; Yu, P. Y. Temperature Dependence of the Free Excitons in a CdS Single Crystal. *J. Korean Phys. Soc.* **2000**, *36*, 102–105.

57. Pan, D. C.; Wang, Q.; Pang, J. B.; Jiang, S. C.; Ji, X. L.; An, L. J. Semiconductor "Nano-Onions" with Multifold Alternating CdS/CdSe or CdSe/CdS Structure. *Chem. Mater.* **2006**, *18*, 4253–4258.

58. Pan, A. L.; Liu, R. B.; Zhang, Q. L.; Wan, Q.; He, P. B.; Zacharias, M.; Zou, B. S. Fabrication and Red-Color Lasing of Individual Highly Uniform Single-Crystal CdSe Nanobelts. *J. Phys. Chem. C* **2007**, *111*, 14253–14256.

59. Yan, H. Q.; Johnson, J.; Law, M.; He, R. R.; Knutsen, K.; Mckinney, J. R.; Pham, J.; Saykally, R.; Yang, P. D. ZnO Nanoribbon Microcavity Lasers. *Adv. Mater.* **2003**, *15*, 1907–1911.

60. Qian, G. X.; Huo, K. F.; Fu, J. J.; Hung, T. F.; Chu, P. K. *In Situ* Growth of Aligned CdS Nanowire Arrays on Cd Foil and Their Optical and Electron Field Emission Properties. *J. Appl. Phys.* **2008**, *104*, 014312.

61. Li, L.; Fang, X. S.; Chew, H. G.; Zheng, F.; Liew, T. H.; Xu, X. J.; Zhang, Y. X.; Pan, S. S.; Li, G. H.; Zhang, L. D. Crystallinity-Controlled Germanium Nanowire Arrays: Potential Field Emitters. *Adv. Funct. Mater.* **2008**, *18*, 1080–1088.

62. She, J. C.; Xiao, Z. M.; Yang, Y. H.; Deng, S. Z.; Chen, J.; Yang, G. W.; Xu, N. S. Correlation between Resistance and Field Emission Performance of Individual ZnO One-Dimensional Nanostructures. *ACS Nano* **2008**, *2*, 2015–2021.

63. Gautam, U. K.; Fang, X. S.; Bando, Y.; Zhan, J. H.; Golberg, D. Synthesis, Structure, and Multiply Enhanced Field-Emission Properties of Branched ZnS Nanotube−In Nanowire Core−Shell Heterostructures. *ACS Nano* **2008**, *2*, 1015–1021.

64. Zhong, D. Y.; Zhang, G. Y.; Liu, S.; Sakurai, T.; Wang, E. G. Universal Field-Emission Model for Carbon Nanotubes on a Metal Tip. *Appl. Phys. Lett.* **2002**, *80*, 506–508.

65. Li, C.; Fang, G. J.; Liu, N. S.; Li, J.; Liao, L.; Su, F. H.; Li, G. H.; Wu, X. G.; Zhao, X. Z. Structural, Photoluminescence, and Field Emission Properties of Vertically Well-Aligned ZnO Nanorod Arrays. *J. Phys. Chem. C* **2007**, *111*, 12566–12571.

66. Xue, X. Y.; Li, L. M.; Yu, H. C.; Chen, Y. J.; Wang, E. G.; Wang, T. H. Extremely Stable Field Emission from AlZnO Nanowire Arrays. *Appl. Phys. Lett.* **2006**, *89*, 043118.

67. Zhai, T. Y.; Dong, Y.; Wang, Y. B.; Cao, Z. W.; Ma, Y.; Fu, H. B.; Yao, J. N. Size-Tunable Synthesis of Tetrapod-like ZnS Nanopods by Seed-Epitaxial Metal-Organic Chemical Vapor Deposition. *J. Solid State Chem.* **2008**, *181*, 950–956.

68. Barrelet, C. J.; Wu, Y.; Bell, D. C.; Lieber, C. M. Synthesis of CdS and ZnS Nanowires Using Single-Source Molecular Precursors. *J. Am. Chem. Soc.* **2003**, *125*, 11498–11499.

69. Hsu, Y. J.; Lu, S. Y.; Lin, Y. F. One-Step Preparation of Coaxial CdS-ZnS and Cd$_{1-x}$Zn$_x$S-ZnS Nanowires. *Adv. Funct. Mater.* **2005**, *15*, 1350–1357.